

Quantification of confounding factors in MRI-based dose calculations as applied to prostate IMRT

This content has been downloaded from IOPscience. Please scroll down to see the full text.

2017 Phys. Med. Biol. 62 948

(<http://iopscience.iop.org/0031-9155/62/3/948>)

View [the table of contents for this issue](#), or go to the [journal homepage](#) for more

Download details:

IP Address: 143.121.237.84

This content was downloaded on 10/03/2017 at 15:58

Please note that [terms and conditions apply](#).

You may also be interested in:

[Generation of synthetic CT data using patient specific daily MR image data and image registration](#)

Kim Melanie Kraus, Oliver Jäkel, Nina I Niebuhr et al.

[MRI-based IMRT planning for MR-linac: comparison between CT- and MRI-based plans for pancreatic and prostate cancers](#)

Phil Prior, Xinfeng Chen, Maikel Botros et al.

[MRI simulation: end-to-end testing for prostate radiation therapy using geometric pelvic MRI phantoms](#)

Jidi Sun, Jason Dowling, Peter Pichler et al.

[A voxel-based investigation for MRI-only radiotherapy of the brain using ultra short echo times](#)

Jens M Edmund, Hans M Kjer, Koen Van Leemput et al.

[MRI-based treatment planning for prostate cancer](#)

L Chen, R A Price Jr, T-B Nguyen et al.

[Radiotherapy planning using MRI](#)

Maria A Schmidt and Geoffrey S Payne

[Atlas-guided generation of pseudo-CT images for MRI-only and hybrid PET–MRI-guided radiotherapy treatment planning](#)

Hossein Arabi, Nikolaos Koutsouvelis, Michel Rouzaud et al.

[A female pelvic bone shape model for air/bone separation in support of synthetic CT generation for radiation therapy](#)

Lianli Liu, Yue Cao, Jeffrey A Fessler et al.

Quantification of confounding factors in MRI-based dose calculations as applied to prostate IMRT

Matteo Maspero¹, Peter R Seevinck¹, Gerald Schubert²,
Michaela A U Hoesl¹, Bram van Asselen¹, Max A Viergever¹,
Jan J W Lagendijk¹, Gert J Meijer¹ and
Cornelis A T van den Berg¹

¹ Universitair Medisch Centrum Utrecht, Center for Image Sciences, Heidelberglaan 100, 3584 CX, Utrecht, The Netherlands

² Philips Healthcare, MR-Therapy, Ayritie 4, PL 185, 01511 Vantaa, Finland

E-mail: m.maspero@umcutrecht.nl

Received 22 September 2016, revised 11 November 2016

Accepted for publication 23 November 2016

Published 11 January 2017



CrossMark

Abstract

Magnetic resonance (MR)-only radiotherapy treatment planning requires pseudo-CT (pCT) images to enable MR-based dose calculations. To verify the accuracy of MR-based dose calculations, institutions interested in introducing MR-only planning will have to compare pCT-based and computer tomography (CT)-based dose calculations. However, interpreting such comparison studies may be challenging, since potential differences arise from a range of confounding factors which are not necessarily specific to MR-only planning. Therefore, the aim of this study is to identify and quantify the contribution of factors confounding dosimetric accuracy estimation in comparison studies between CT and pCT. The following factors were distinguished: set-up and positioning differences between imaging sessions, MR-related geometric inaccuracy, pCT generation, use of specific calibration curves to convert pCT into electron density information, and registration errors.

The study comprised fourteen prostate cancer patients who underwent CT/MRI-based treatment planning. To enable pCT generation, a commercial solution (MRCAT, Philips Healthcare, Vantaa, Finland) was adopted. IMRT plans were calculated on CT (gold standard) and pCTs. Dose difference maps in a high dose region (CTV) and in the body volume were evaluated, and the contribution to dose errors of possible confounding factors was individually quantified.

We found that the largest confounding factor leading to dose difference was the use of different calibration curves to convert pCT and CT into electron density (0.7%). The second largest factor was the pCT generation

which resulted in pCT stratified into a fixed number of tissue classes (0.16%). Inter-scan differences due to patient repositioning, MR-related geometric inaccuracy, and registration errors did not significantly contribute to dose differences (0.01%).

The proposed approach successfully identified and quantified the factors confounding accurate MRI-based dose calculation in the prostate. This study will be valuable for institutions interested in introducing MR-only dose planning in their clinical practice.

Keywords: magnetic resonance, radiotherapy planning, dosimetry, MR-only treatment planning, intensity modulated radiotherapy, quality assurance

 Online supplementary data available from stacks.iop.org/PMB/62/948/mmedia

(Some figures may appear in colour only in the online journal)

1. Introduction

In external beam radiotherapy, computed tomography (CT) is the primary imaging modality for treatment planning (Chernak *et al* 1975, Pereira *et al* 2014), since it enables precise calculation of dose distributions (Seco and Evans 2006, Skrzyński *et al* 2010, Brock and Dawson 2014), and provides reference images allowing for pre-treatment positioning (Van den Berge *et al* 2000).

In the last few decades, magnetic resonance imaging (MRI) has found its way into the radiotherapy workflow as it provides superior soft tissue contrast with respect to CT (Debois *et al* 1999, Dirix *et al* 2014), thus enabling more accurate delineation of target regions and critical structures (Roach *et al* 1996, Rasch *et al* 1999, Villeirs *et al* 2005).

To benefit from the advantages offered by both imaging modalities, MR images are nowadays fused to CT images to transfer target and organ at risk contours (Khoo *et al* 1997, Paulson *et al* 2015, Schmidt and Payne 2015). However, image fusion potentially causes systematic spatial uncertainties and introduces errors during radiotherapy treatment planning (Karlsson *et al* 2009, Nyholm *et al* 2009). To minimise these uncertainties and errors, an MR-only based workflow has been proposed (Fraass *et al* 1987, Lee *et al* 2003, Nyholm and Jonsson 2014), aiming at prevention of inter-modality registration errors (Nyholm *et al* 2009). Furthermore, an MR-only based workflow will result in practical and logistical advantages: it can simplify the workflow and reduce the overall treatment cost (Devic 2012) and workload (Karlsson *et al* 2009), and it can decrease exposure to ionising radiation, which is particularly important when several replans have to be made (Kapanen *et al* 2013).

Additionally, based on the growing importance of the exclusive use of MRI in radiotherapy (Raaymakers *et al* 2004, Dempsey *et al* 2005, Fallone *et al* 2009, Karlsson *et al* 2009), we foresee that MR-based dose calculations will also be of increasing importance to radiotherapy.

The main obstacle regarding the introduction of MR-only radiotherapy is the lack of tissue attenuation information, which is required for accurate dose calculations (Nyholm *et al* 2009, Jonsson *et al* 2010). To estimate tissue attenuation properties from MRI, several methods have been proposed in the last few decades (Lee *et al* 2003, Chen *et al* 2004, Schmidt and Payne 2015, Prior *et al* 2016). More recently, MRI vendors have launched solutions as well (Schadewaldt *et al* 2014, Siversson *et al* 2015). The proposed methods can be categorised into three classes (Prior *et al* 2016): (1) atlas-based, (2) voxel-based or (3) bulk assignment-based

techniques. Along with these techniques, several names have been used all referring to MR-based tissue attenuation maps, e.g. synthetic-CT (Kim *et al* 2015, Siversson *et al* 2015), pseudo-CT (Dowling *et al* 2012, Korhonen *et al* 2014), and substitute-CT (Johansson *et al* 2012). For clarity, without differentiating among generation techniques, the term ‘pseudo-CT’ (pCT) will be used to refer to the tissue attenuation equivalent images, and ‘pseudo-HU’ to indicate the assigned Hounsfield unit (HU) values.

An institution interested in introducing an MR-only planning solution into the clinic will face the challenge of determining the accuracy of the MR-based dose planning with respect to the gold standard CT planning (Korsholm *et al* 2014, Schmidt and Payne 2015). Based on the quantitative outcome of a comparison study an institute should decide whether the accuracy of MR-based planning is acceptable. Very likely, such a comparison study may result in observed dose differences (Lee *et al* 2003, Chen *et al* 2004, Dowling *et al* 2012, Johansson *et al* 2012, Korhonen *et al* 2014, Schadewaldt *et al* 2014, Kim *et al* 2015, Siversson *et al* 2015, Prior *et al* 2016). To understand and gauge the potential impact of these differences, and thus, possibly facilitate institutions to reduce them (reducing in this way overall treatment inaccuracies), it is important to understand their origin. Differences may have origin other than the adopted pCT generation technique (Siversson *et al* 2015, Sun *et al* 2015). In particular, considering the treatment planning workflow, such differences originate from the following processes: image acquisition, image processing for pCT generation, and dose calculations. In each individual process we hypothesise that at least one among the following four ‘confounding factors’ will contribute to the observed dose differences between plan generated using CT and pCT:

- (1) **Set-up & positioning differences.** During image acquisition the patient is repositioned between CT and MR imaging sessions. To minimise possible positioning differences between imaging sessions, the use of a flat table top (Mcjury *et al* 2011), coil supports (Kapanen *et al* 2013, Sun *et al* 2014), and positioning devices such as lasers (Schmidt and Payne 2015) at MR scanner (and also CT scanner) are generally used. We refer to this set-up configuration as ‘MR simulator’. However, even if an MR simulator is employed, differences in patient positioning, and possible set-up errors may occur (van Herk *et al* 1995).
- (2) **MR-related geometric inaccuracy.** MR image acquisition may be compromised by geometric distortions caused by the system and/or patient (Fransson *et al* 2001, Walker *et al* 2014). Modern scanners are equipped with solutions (Schmidt and Payne 2015) that limit system-related displacements to 2–3 mm on the outer edges of a clinically relevant volume of approximately $25 \times 25 \times 25 \text{ cm}^3$ (Wang *et al* 2004). Patient-related distortion may be mitigated by careful choice of scan parameters, e.g. bandwidth and slice thickness, ensuring spatial geometric accuracy of MR images (Stanescu *et al* 2012). Nonetheless, residual distortions may still be among the potential factors that confound the accuracy of pCT-based dose calculations.
- (3) **Pseudo-CT generation.** This factor solely originates from the pCT generation method used. All the pCT generation techniques (atlas-based, voxel-based or bulk assignment-based) assign HU voxel values that may differ with respect to the corresponding voxel on CT (assuming spatial relationship), thus contributing to observed dose differences.
- (4) **Electron density conversion.** To enable dose calculations, electron density information is derived from tissue attenuation equivalent data (CT or pCT). In particular, for radiotherapy planning, each CT scanner is calibrated such that HU can be converted into electron density by using a calibration curve derived from literature (Knöös *et al* 1986, IAEA 2008), or by using a one-to-one relationship obtained from a phantom made of tissue equivalent

materials (Constantinou *et al* 1992). The use of different phantoms (usually the phantoms differ in the high HU region due to the use of slightly different bone-like materials) to calibrate CT scanners can result in dose differences up to 1% (Thomas 1999). If a pCT generation method assigns HU, it may implicitly assume also a certain calibration curve for electron density conversion (Lee *et al* 2003, Jonsson *et al* 2010, Lambert *et al* 2011). The assumed conversion curve may differ from the one clinically adopted for CT images, thus contributing to observed dose differences.

Moreover, when comparing the output of dose calculations, another factor could contribute to observed dose differences:

- (5) **Registration errors.** During dose comparisons it may be necessary to align the spatial coordinates of CT and pCT. When registrations are performed, registration errors may play a role in differences between doses calculated on CT and pCT (Roberson *et al* 2005, Nyholm *et al* 2009).

Factors (1), (2) and (5) together with internal motion may result in *inter-scan differences* between imaging sessions in the case that one session is performed at an MR scanner.

This work aims to quantify the possible contributions of *inter-scan differences* (as combination of 1, 2 and 5), *pseudo-CT generation* (3), and *electron density conversion* (4) to dose differences between CT- and pCT-based dose calculations. The effects of the different factors were isolated by the specific design of the approach: CT-based pCTs were generated to circumvent the presence of inter-scan differences, as these differences are independent of the pseudo-HU values assigned by the pCT generation method. This study will focus on the pelvic area, with particular attention to prostate radiotherapy treatments.

2. Materials and methods

We conducted a study using data from prostate cancer patients undergoing external beam radiotherapy to compare CT/MR-based and MR-only based dose calculations. The study is divided into five parts. First, we acquired CT and MR images (section 2.1). Second, we generated a series of CT- and MR-based pCTs which allows disentanglement of the confounding factors hypothesised in section 1 (section 2.2). Third, we performed dose planning on pCT images (section 2.3). Fourth, we evaluated the body contour differences between the CT-based and MR-based pCTs (section 2.4). Finally, we quantified the impact of possible confounding factors on dose calculations (section 2.5).

2.1. Patient data collection

In the first part of the study we collected data of fourteen prostate cancer patients (57.7–80.2 years old) who underwent standard treatment planning between November and December 2015. As part of the treatment planning, gold fiducial markers (HA2 Medizintechnik GmbH, Germany) were transperineally implanted for position verification purposes one week before acquisition of planning images. The data collection was conducted following the local statutory requirements, and in accordance with the local medical ethical guidelines.

Image acquisition. The patients underwent a CT scan (Brilliance CT Big Bore Oncology, Philips Healthcare, Best, The Netherlands—figure 1(a)) and a 3 T MR scan (Ingenia—70 cm wide bore, Philips Healthcare, Best, The Netherlands—figure 1(b)) as part of clinical treatment planning.

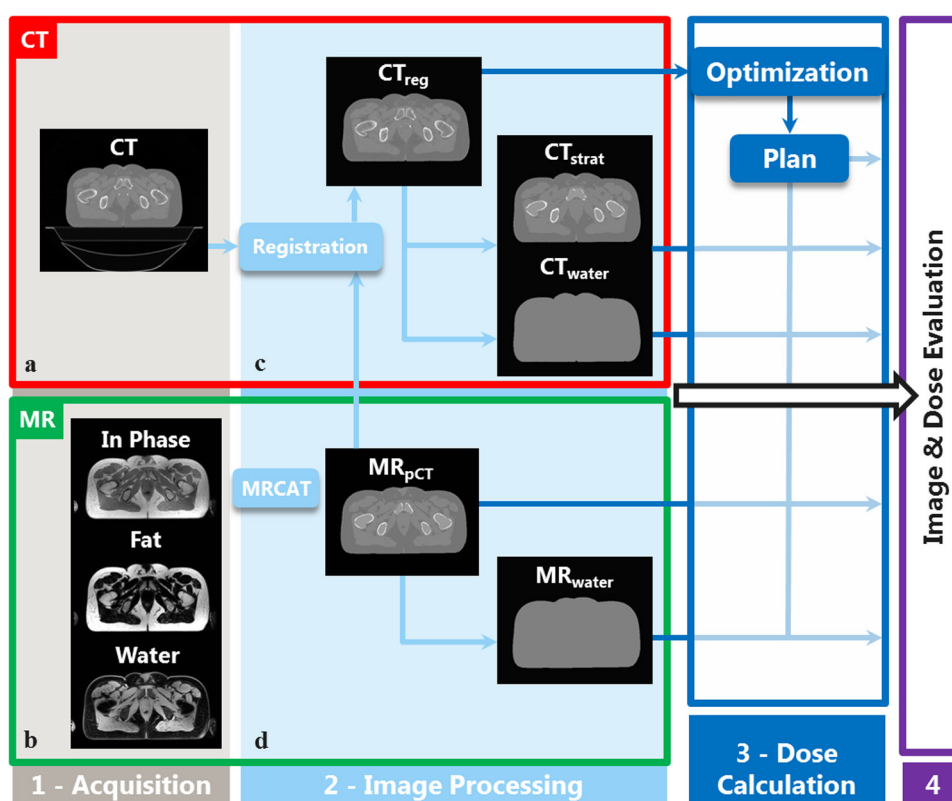


Figure 1. Schematic of the study. After patient data collection (1) on CT (a) and MR (b), via image processing (2) three CT-based pCT datasets (c), and two MR-based pCT datasets (d) were produced. CT-based pCT generation (c) was performed after image registration and couch removal (CT_{reg}) to obtain a dataset similar to MR_{pCT} (CT_{strat}) and a homogeneous water density dataset (CT_{water}). MR-based pCTs (d) were generated using the *MRCAT* method (MR_{pCT}), and, from its body contour, a homogeneous water density dataset (MR_{water}) was created. Planning and dose calculations (3) followed the pCT generation, and finally image and dose evaluation (4) was performed to disentangle and quantify possible confounding factors.

CT scans were performed with the following imaging parameters: 120 kV, exposure time = 923 ms, tube current between 121 and 183 mA, in-plane matrix of 512×512 pixels, and 3 mm slice thickness. The resolution was variable depending on the field of view (FOV) used. The typical size of the FOV was $500 \times 500 \times 300 \text{ mm}^3$, which corresponds to an in-plane resolution of $0.98 \times 0.98 \text{ mm}^2$.

MR scans were carried out 1–2 h after CT scans. To simulate treatment positioning, the patients were marked with three skin tattoos at the CT scanner, and the position of the tattoos was used to reposition the patient at the MR scanner. To facilitate patient positioning, the MR scanner was equipped with an external laser positioning device (Dorado 3, LAP GmbH Laser Applikationen, Lueneburg, Germany), and an in-house-built flat table top. Patients were scanned using anterior and posterior coils (dS Torso and Posterior coils, Philips Healthcare, Best, The Netherlands). To avoid compression of patients, two in-house-built coil bridges supported the anterior coil.

Table 1. The pseudo-HU assigned to the five tissue classes of MR_{pCT}, together with the ranges used during the stratification of CT_{reg} (i.e. the generation of CT_{strat}).

Classes	Pseudo-HU (HU)	Range stratification (HU)
Outside air	−968	(−∞; −200]
Fat	−86	(−200; 28.5]
Muscle	42	(−28.5; 100]
Spongy bone	198	(100; 575]
Compact bone	949	(575; ∞)

To generate MR-based pCTs, a two echoes 3D Cartesian radio frequency spoiled gradient echo sequence was added to the standard MR exam. In particular, two images were acquired with the following imaging parameters: echo times = 1.21/2.53 ms, repetition time = 3.93 ms, flip angle = 10°, FOV = 477 × 477 × 300 mm³, acquisition matrix = 248 × 281 × 120, reconstructed matrix = 480 × 480 × 120, bandwidth = 1083 Hz, and acquisition time of 2 min 13 s. A Dixon (Dixon 1984) reconstruction (Eggers *et al* 2011) was performed to obtain in-phase, fat, and water images (figure 1(b)).

2.2. Image processing for pCT generation

In the second part of the study, we generated five image datasets (figures 1(c) and (d)) comprising two pCTs based on MR data (figure 1(c)), one registered CT, and two pCTs based on CT data (figure 1(d)), for all fourteen patients. Each pCT dataset was generated with a specific goal, as described below.

To enable MR-only dose planning, we generated pCTs using a vendor solution tailored to prostate patients which is called MR for attenuation correction (*MRCAT* prototype rev. 257, Philips Healthcare, Vantaa, Finland). *MRCAT* is a bulk assignment pCT generation method based on sequential intensity- and model-based segmentation techniques (Schadewaldt *et al* 2014). In particular, *MRCAT* segments images from a dedicated MR sequence (see section 2.1) into five classes, and assigns to each class the pseudo-HU specified in table 1. *MRCAT* uses a constrained shape model to estimate body contour and to segment bone structures. Within the bone structures two classes are assigned: spongy and compact bone. Similarly, soft tissue structures are assigned either fat or muscle. *MRCAT* does not recognise gold fiducial markers implanted in the patients, and classifies them as soft tissue. Furthermore, *MRCAT* produces images with no air compartments within the body contour. As *MRCAT* converts pseudo-HU in electron density using a vendor specific curve, *MRCAT* can be considered an electron density map generation method. The term MR_{pCT} (figure 1(d)) was used to refer to the dataset produced by *MRCAT*.

To align the spatial coordinates of the CT with the MR, and to minimise positioning errors, the CT was rigidly registered and resampled to the MR_{pCT}. We considered MR_{pCT} as a fixed image to prevent changes of the pseudo-HU values during the resampling. A multi-resolution registration with a mutual information metric was performed in Elastix (Klein *et al* 2009, 2010). The parameter file used has been stored on <http://elastix.bigr.nl/wiki/>.

To enable planning, the delineations used in the clinical plan were propagated to the registered CT, and the CTV was propagated to MR_{pCT}. To further minimise differences between CT and MR, the couch in the CT images was removed by assigning the value −968 HU outside body contour. Body contour detection was performed using an intensity threshold of −200 HU. We refer to the resulting dataset as CT_{reg}.

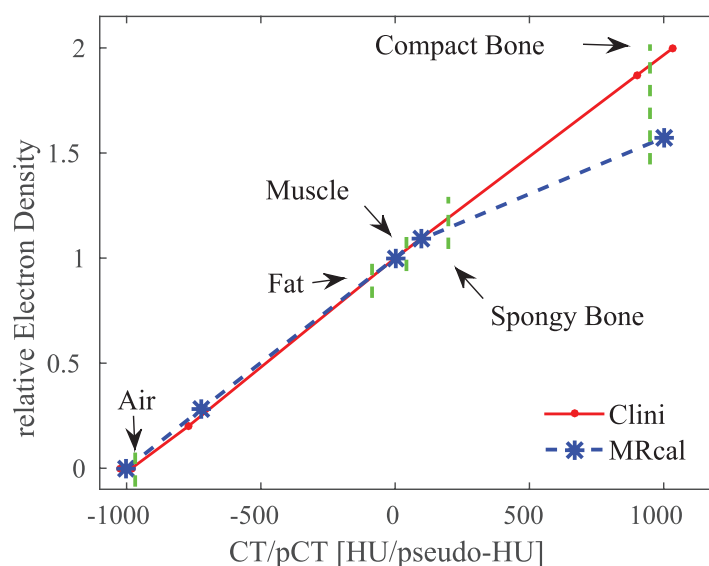


Figure 2. Calibration curves used to convert CT or pCT in relative electron density. The (red) straight curve, called *Clini*, is used in our institute and based on the Catphan (The Phantom Laboratory, Greenwich, New York, USA) phantom, while the (blue) dashed curve, called *MRcal*, has been provided along with the *MRCAT* method and based on literature (ICRU 1989, 1992). The (green) vertical dashed line corresponds to the pseudo-HU used in the *MRCAT* method, as presented in table 1.

To quantify *set-up & positioning differences*, *MR-related geometric inaccuracy*, and *registration errors* (referred to as *inter-scan differences*), homogeneous water density CT- and MR-based pCTs were generated. In particular, the entire body volume of CT_{reg} and MR_{pCT} were considered being water-equivalent (pseudo-HU = 0) after thresholding the images at -200 HU. We refer to these datasets as CT_{water} and MR_{water} , respectively. For clarity, the only difference between both datasets is the body outline.

To quantify the *pseudo-CT generation* factor, we aimed to circumvent *inter-scan differences* by producing CT-based pCTs similar to MR_{pCT} . More specifically, we stratified the registered CT by assigning the same pseudo-HU values as employed in *MRCAT* to the different tissue classes. First, the voxels of CT_{reg} were separated into five classes according to the ranges shown in table 1. These ranges were chosen by adjusting the values proposed by Helle *et al* (2014). Second, since MR_{pCT} has no air in the body region, air pockets within the body outline were classified as fat. Third, since no soft tissue is present within bone regions of MR_{pCT} , all voxels that were labelled as soft tissue and surrounded by spongy or compact bone regions were reclassified as spongy bone. To do so, a morphological closing filter was used. As a final step, the lack of gold fiducial marker on MR_{pCT} was emulated: the voxels in the CTV classified as bone were reclassified as muscle. We use the term CT_{strat} to refer to this dataset. In appendix A, we show that CT_{strat} can be used to quantify the contribution of the *pseudo-CT generation* confounding factor.

Before planning, CTV delineations were propagated to CT-based pCTs. CT (a) and MR (b) images of one of the patients, together with the five corresponding datasets ((c) and (d)) are shown in figure 1.

The code used to generate CT_{reg} , CT_{strat} , and CT_{water} has been made publicly available at https://matteomaspero.github.io/pseudo-CT_generation/.

2.3. Treatment planning

In the third part of the study, intensity modulated radiotherapy (IMRT) plans, using 5 beams of 10 MV, were generated for each patient using a Monte Carlo-based treatment planning system (Monaco v5.10.00, Elekta AB, Stockholm, Sweden). The plan isocentre was the centre of gravity of the CTV. The beam angles were fixed: 40°, 100°, 180°, 260°, and 320° (considering 0° the anterior direction and rotating clockwise). The prescribed mean dose to the entire prostate gland was 77 Gy. Plan optimisation was carried out on CT_{reg} to fulfil clinical requirements (described by Lips *et al* (2008)). Dose calculations were performed on a 3 mm³ grid and 1% statistical uncertainty per control point.

To eliminate the dose differences that could arise during separated optimisation procedures, the plans were recalculated on each pCT dataset keeping the planning parameters, i.e. beam energies, angles, photon fluency, and monitor units unchanged.

The vendor of *MRCAT* provided a calibration curve to convert pseudo-HU into electron density adapted from literature (ICRU 1989, 1992). We refer to this calibration curve as *MRcal*. In our institution, a different calibration curve is currently used, which is a curve obtained with a Catphan phantom (The Phantom Laboratory, Greenwich, New York, USA) for CT scanner calibration. We refer to this curve as *Clini*. To investigate the impact of these different calibration curves on dose calculations (referred to as the *electron density conversion factor*), dose calculations using both calibration curves were carried out. Figure 2 depicts both the *MRcal* and *Clini* curve.

2.4. Evaluation of inter-scan differences

In the fourth part of our study, we investigated inter-scan differences due to possible *set-up & positioning differences*, *MR-related geometric inaccuracy*, and *registration errors*. More specifically, we took into consideration body contour differences of MR and CT. The body contour may be affected by set-up errors and patient repositioning that occurs during different imaging sessions. Additionally, the body contour is the anatomical region expected to be maximally influenced by MR geometric distortion, considering that distortion radially increases from the scan isocentre (Baldwin *et al* 2007). For these reasons, we considered the beam depth difference between MR_{pCT} and CT_{reg} as an estimate for inter-scan differences. Here, the beam depth is defined as the radial distance between isocentre and body contour. The definition of isocentre is dependent on the registration between image modalities. Note that, as specified in the introduction, when referring to inter-scan differences we consider also potential image registration errors.

We evaluated inter-scan variability in terms of beam depth of the five beam angles and in all radial directions. The beam depth of the five beams was directly extracted from each control point of the IMRT plans. The beam depth in all the radial directions was obtained by planning a single 10 MV 360° arc in Monaco and linearly interpolating at 1° intervals the radial beam depth extracted from the control points of the plan.

For each patient, the mean of the beam depth difference between CT_{reg} and MR_{pCT} over a complete 360°-arc, and over the five beams were estimated. Figure 3 shows an example of the radial representation of the beam depth (top) over a complete 360°-arc, and the beam depth difference between CT_{reg} and MR_{pCT} (bottom) for one of the patients.

The average and standard deviation (SD) over the whole population of the mean beam depth differences for the five beams and in all the radial directions were calculated. Single sample t-tests at $p = 0.01$ significance level were also conducted.

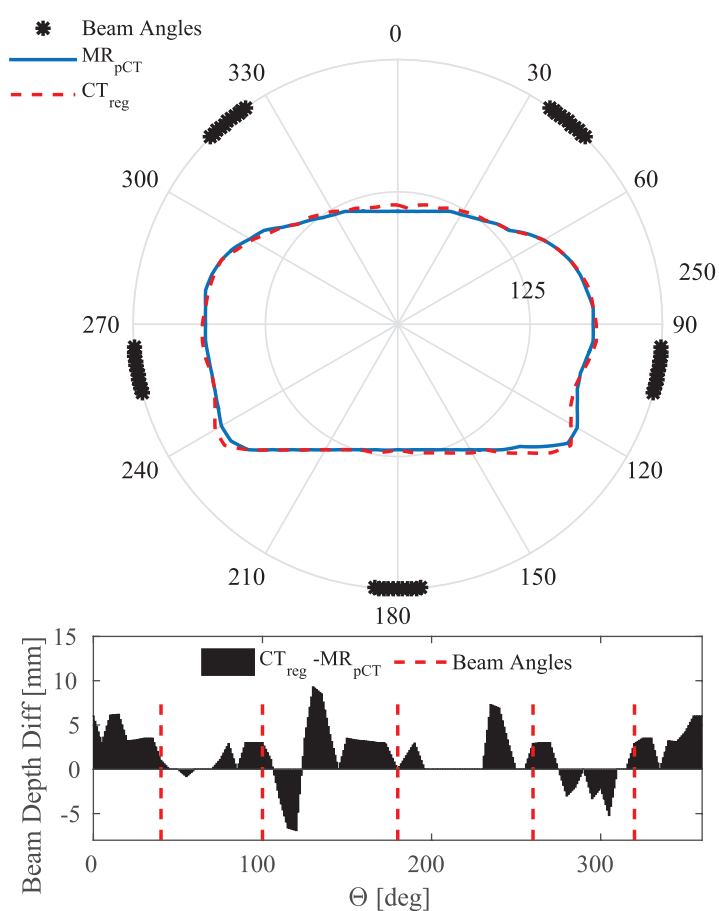


Figure 3. (Top) Beam depth (in mm) from isocentre to body contour of MR_{pCT} (blue continuous line) and CT_{reg} (red dashed line) for one patient. (Bottom) Difference between beam depth on CT_{reg} and MR_{pCT} in all the directions as function of the beam angle Θ for the shown patient. The location of the five beam angles is also represented as a 10° arc in the polar plot (top) and as vertical dashed (red) lines in the bar plot (bottom).

2.5. Dosimetric evaluation

Lastly, we carried out a dosimetric evaluation to quantify the relative contribution of the three confounding factors (*inter-scan differences*, *pseudo-CT generation* and *electron density conversion*). To estimate their dosimetric contributions, the voxel-by-voxel relative percentage dose difference (RelDiff) between two pCTs was calculated as follows:

$$\text{RelDiff}(\%) = \frac{\text{Test} - \text{Ref}}{\max(\text{Ref})} * 100$$

where $\max(\text{Ref})$ refers to the maximum dose value of Ref of each patient. To disentangle the individual confounding factors, we considered Ref and Test dose distributions as here presented:

- **Inter-scan differences.** CT_{water} and MR_{water} differ only due to *set-up & positioning differences* and *MR-related geometric inaccuracy*, and *registration errors* (inter-scan differences) when the dose calculation is performed using the same calibration curve (*Clini* in this case). The ‘inter-scan differences’ factor was estimated by considering CT_{water} as Ref and MR_{water} as Test.
- **Pseudo-CT generation.** CT_{strat} is immune to inter-scan differences with respect to CT_{reg} . To estimate the ‘pseudo-CT generation’ factor, we considered CT_{reg} as Ref and CT_{strat} as Test converting pseudo-HU into electron density with the *Clini* calibration curve for both datasets.
- **Electron density conversion.** To estimate the ‘electron density conversion’ factor, we considered the dose on CT_{reg} planned with the *Clini* calibration curve as Ref and the dose on CT_{reg} planned with the *MRcal* as Test.

To estimate the systematic contribution and error of each confounding factor, we calculated the average and SD among all the patients of the mean RelDiff in the CTV and in the V_{Body} . The CTV was considered to represent the high dose region (where the largest dose difference is expected to be found), while the V_{Body} was considered to represent the largest anatomical region common to MR- and CT-based pCTs (CTV included). V_{Body} was defined as intersection of the body contour of the MR_{pCT} and the CT_{reg} . The resulting contour was isotropically eroded by 1.5 cm in each transverse slice to exclude build-up regions which are compromised by a steep dose gradient.

We also investigated the scenario taking into account the sum of **all** the **factors**, by considering CT_{reg} as Ref and MR_{pCT} as Test. Here, we considered two scenarios: one with different electron density conversions (*Clini* and *MRcal*), and one with the same electron density conversion (both *MRcal*). A third possible scenario (same electron density conversion: both *Clini*) has not been considered since the vendor suggests the use of MR_{pCT} in combination with *MRcal*. For these scenarios, we performed the same statistical analysis as described above.

3. Results

3.1. Evaluation of inter-scan differences

The beam depth difference (CT_{reg} minus MR_{pCT}) was 0.9 ± 0.7 mm (1 SD, $p < 0.01$), and 0.2 ± 1.5 mm ($p = 0.63$) when calculated over the complete 360°-arc and the five beam angles, respectively.

As shown in figure 4 considering the average (and SD) of the beam depth differences between CT_{reg} and MR_{pCT} over all patients for the complete 360°-arc, the largest variations of beam depth differences occur at Θ about 130° and 240°. These angles correspond to the locations where the patient contour is not in contact with the flat table top, as figure 3 (top) clearly illustrates. As this trend is seen after averaging over fourteen patients, the large variations may relate to a systematic positioning error, e.g. due to inclination of the in-house-built flat table top at MR, or due to a systematically different positioning of the patient legs between CT and MR imaging sessions.

3.2. Dosimetric evaluation

A summary of the quantification of confounding factors described in section 2.4 is reported in table 2 as means (± 1 SD) over all fourteen patients in view of mean RelDiff to CTV and V_{Body} .

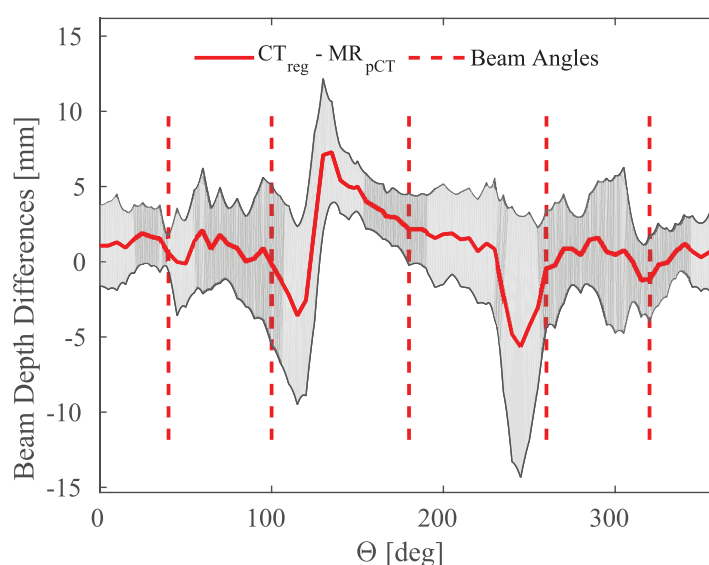


Figure 4. Beam depth (in mm) difference in all radial directions between CT_{reg} minus MR_{pCT} as an average over the patient population. The (red) continuous line and the grey region indicate the average and the SD over the patient population, respectively. The five beam angles are represented by vertical (red) dashed lines.

Table 2. Confounding factors estimation in terms of average relative dose difference (RelDiff \pm 1 SD) over all patients for CTV and V_{Body} between the test and ref datasets. The calibration curves to convert the test and ref datasets (*MRcal* or *Clini*) into electron density are indicated in the columns ‘calibration’.

pCTs compared		Calibration		Confounding factors	RelDiff \pm 1 SD (%)	
Ref	Test	Ref	Test		CTV	V_{Body}
CT_{reg}	MR_{pCT}	<i>Clini</i>	<i>MRcal</i>	All factors	1.0 ± 0.6	0.14 ± 0.07
		<i>MRcal</i>	<i>MRcal</i>		0.33 ± 0.39	0.04 ± 0.06
CT_{reg}	CT_{reg}	<i>Clini</i>	<i>MRcal</i>	ED conversion	0.7 ± 0.2	0.10 ± 0.03
CT_{reg}	CT_{strat}	<i>Clini</i>	<i>Clini</i>	Pseudo-CT generation	0.16 ± 0.13	-0.03 ± 0.02
CT_{water}	MR_{water}	<i>Clini</i>	<i>Clini</i>	Inter-scan differences	0.01 ± 0.35	0.00 ± 0.06

Considering ‘all factors’ combined (first two rows of table 2), the electron density conversion on CT_{reg} and MR_{pCT} was carried out using the *Clini* and *MRcal* calibration curve, respectively. We found (first row of table 2) a dose overestimation of $1.0 \pm 0.6\%$ (1 SD) when considering the overall dose difference (MR_{pCT} minus CT_{reg}). The observed dose overestimation more than halved when omitting the *electron density conversion* factor (second row of table 2): the average RelDiff between CT_{reg} and MR_{pCT} was $0.33 \pm 0.39\%$ when the electron density conversion was performed using the *MRcal* calibration curve for both datasets. The

dose comparison considering all the factors (first and second rows of table 2) for each patients is reported in the supplementary material (stacks.iop.org/PMB/62/948/mmedia).

When comparing the possible confounding factors separately, the *electron density conversion* (row three of table 2) was found to contribute the largest relative dose difference ($0.7 \pm 0.2\%$), followed by the *pseudo-CT generation* (row four of table 2) into five bulk-assigned tissue classes ($0.16 \pm 0.13\%$). For these two confounding factors the dose difference was within two SDs to zero.

The *set-up & positioning differences* and *MR-related geometric inaccuracy* (last row of table 2) were the only confounding factors within one SD to zero: the average RelDiff was $0.01 \pm 0.35\%$ between CT_{water} and MR_{water} in the CTV.

4. Discussion

In radiotherapy, a high level of accuracy is required to deliver clinically effective treatments (Mijnheer *et al* 1987, Thwaites 2013). To comply with such a requirement, institutions interested in introducing an MR-only workflow into their clinic should evaluate whether (and how) MR-planning impact the geometric and dosimetric accuracy of the radiotherapy treatment.

As part of such an evaluation, the present study was designed to verify the accuracy of MR-only dose calculations focusing on the case of prostate cancer patients. Additionally, we were interested in disentangling factors which may confound the results of this evaluation and that were described in the introduction (section 1). The key aspect of our approach was the generation of a series of CT-based pCTs to circumvent the intrinsic geometrical distortions in MRI, possible set-up and positioning differences, and registration errors (so called inter-scan differences). This allowed the quantification of the sole effect of the pseudo-CT generation technique. More specifically, we compared CT-based dose calculations to MR-only based dose calculations that were enabled by a commercially available solution known as *MRCAT* (Philips Healthcare, Vantaa, Finland).

The contribution of the aforementioned confounding factors was successfully identified, finding that the *electron density conversion*, and *pseudo-CT generation* contributed within two SDs of zero to the observed dose differences, while *inter-scan differences* within one SD of zero.

In particular, the largest confounding factor was the *electron density conversion* (0.7% dose difference in the CTV). Note that inaccuracy due the use of different calibration curves to convert HU (or pseudo-HU) in electron density has been already reported in literature as a possible source of inaccuracy in CT-based dose calculations, causing comparable dose differences (Thomas 1999, Inness *et al* 2014). The *electron density conversion* is a factor which is not specific of all pCT generation methods, however the fact that this was the largest contributing factor in our study highlights the importance of its evaluation during the introduction of an MR-only workflow.

The second-largest factor was the *pseudo-CT generation* (0.2% dose difference in the CTV). Siverson *et al* (2015) reported dose differences to the CTV of $0.0 \pm 0.2\%$ between registered CT and MR-based pCTs. Siverson circumvented *inter-scan differences*, employing non-rigid registration, which is a different method to isolate the *pseudo-CT generation* factor with respect to the one adopted in the present study. However, the contribution of the *pseudo-CT generation* to the relative dose difference is consistent with their observation.

When focusing on the impact of *set-up & positioning differences*, *MR-related geometric inaccuracy*, and images *registration errors*, we found that such confounding factors resulted in a dose difference within one SD of zero ($0.01 \pm 0.35\%$). As a result, we concluded that

residual discrepancies in inter-scan body outline between MR and CT imaging sessions did not contribute to the dose inaccuracy when planning with IMRT. Lambert *et al* (2011) quantified *inter-scan differences*, comparing doses planned on homogeneously assigned water-equivalent CT- and MR-based pCTs. The authors observed a dose difference of 1.3%. This difference is larger than what has been found in the present study. However, Lambert *et al* (2011) did not use coil support during MRI. In this way, the skin surface of the patient may be compressed, possibly leading to the larger observed differences. Sun *et al* (2015) showed that external body deformation due to lack of coil support resulted in an observed dose difference of approximately 0.6 Gy, which corresponds to about 0.9% of the prescribed dose. This is comparable with our findings, and shows that the MR-simulator configuration adopted in this study minimises inter-scan differences.

From a geometric perspective, we found differences in body shapes that may originate from an inclination of the in-house built flat table top or from consistently different patient positioning on the CT and MR scanners. Further research will investigate the possible causes taking also into consideration that *MR-related geometric* inaccuracy and registration errors could play a role. In any case, even if systematic set-up errors and incorrect patient positioning may have occurred, contributing to observed beam depth differences, they did not contribute to observed dose differences.

Within our study, we demonstrated that exclusion of the *electron density conversion* factor (planning on the same calibration curve) reduced the difference between CT-based and pCT-based dose calculations from about 1% to 0.3%. In previous work, several authors concluded that comparable, or even higher observed dose differences would enable accurate MR-only dose calculations (Dowling *et al* 2012, Korhonen *et al* 2014, Kim *et al* 2015, Siversson *et al* 2015). We concluded that *MRCAT* enables accurate MR-based dose calculation to the target.

A limitation of the present study is that for each patient a large number of plans (6) needs to be recalculated. In this regard, we believe that the proposed strategy is suitable mainly for initial evaluations of the MR-only workflow.

It would be desirable to show in future work a generalisation of the approach to other pCT generation techniques and anatomies. We believe that the application of the proposed approach is independent of the chosen pCT generation technique. This hypothesis is supported by the fact that the identification of confounding factors relies on the generation of CT-based pCT images that emulate MR-based pCT images: in principle the strategy is not dependent of irradiation modalities, or anatomical locations. Continuing this thought, we foresee as a straightforward possible application the situation in which MR-only planning merely relies on bulk assignment-based pCT generation techniques. Note however that the image processing pipeline to generate CT_{strat} would require optimisations for any pCT generation other than *MRCAT*.

Finally, we would like to underline that the here presented dose accuracy evaluation of an MR-only pCT generation method is not sufficient to introduce MR-only radiotherapy in the clinic. The clinical introduction of MR-only radiotherapy involves more steps, e.g. evaluation of MR-only delineations, and evaluation of MR-based position verification. These steps also contribute to the overall dose delivery accuracy and have to be taken into consideration by institutions interested in MR-only radiotherapy.

5. Conclusion

In this work, factors confounding accurate MRI-based dose calculation in the prostate were identified and quantified. This is a crucial step when aiming to introduce MR-only treatment

planning into the clinic. With this regard, the method presented to quantify the confounding factors will be valuable for institutions interested in introducing MR-only dose planning in their clinical practice.

Acknowledgments

The research is funded by ZonMw IMDI Programme, project number: 104003010. The project is co-funded by Philips Healthcare. The study received approval of the medical ethical commission (Medisch Ethische Toetsings Commissie) and was classified under the protocol number 15-444/C. Peter R Seevinck declares to be a majority shareholder of MRIGuidance BV. Gerald Schubert declares to be employed by Philips Healthcare. Max A Viergever discloses research contracts with Philips Healthcare, and with Pie Medical Imaging BV. Cornelis A T van den Berg declares to be a minority shareholder of MRCode BV. The authors are grateful to Matti Lindstrom and Aleksii Halkola for the support given in terms of pCT generation, and to Sara Hackett for proofreading the manuscript.

Appendix. Evaluation of CT-based pCT similarity

In this section we demonstrate the similarity between the CT-based (CT_{strat}) and the MR-based (MR_{pCT}) pCTs. This will justify using CT_{reg} and CT_{strat} to quantify the contribution of the *pseudo-CT generation* confounding factor. To quantify the similarity we used metrics (1) applicable to any pCT generation technique, and (2) applicable only to bulk assignment-based pCT generation techniques.

(1) MR_{pCT} served as reference for CT_{strat} and CT_{reg} . We assumed that the registration of CT (and CT-based pCTs) minimises *inter-scan differences*. For each patient, mean HU, and mean average error (MAE) was calculated within the body intersection of CT_{strat} and MR_{pCT} (Johansson *et al* 2012, Rank *et al* 2013, Siversson *et al* 2015). MAE was calculated for all N voxels within the body contour as follows:

$$\text{MAE} = \frac{1}{N} \sum_{i=1}^N |pCT_i - MR_{pCT_i}|,$$

The average and standard deviation (SD) of mean HU and MAE over all the patients was considered as representative of similarity among pCTs. We conducted a double sample t-test at $p = 0.01$ significance level on the MAE.

(2) A voxelwise comparison of the tissue classification between CT_{strat} and MR_{pCT} was carried out. Such a comparison was enabled by the voxelwise spatial relationship among CT-based pCTs and MR-based pCTs. We performed (i) a volumetric, and (ii) a classification analysis.

(i) The mean relative volume percentage of each tissue class in the two datasets for each patient was calculated. The average and SD over the whole patient population were reported, and a double sample t-test at $p = 0.01$ significance level was conducted for each class.

(ii) A confusion matrix (Kohavi and Provost 1998) in terms of percentage of the body volume intersection of CT_{strat} and MR_{pCT} was calculated: the tissue class for each voxel of MR_{pCT} was compared to CT_{strat} tissue class, considering the voxels MR_{pCT} as being correctly classified. The average and SD of the confusion matrix were calculated for each combination of classes of CT_{strat} and MR_{pCT} over all the patients. To preliminarily evaluate the impact on the dose, differences in radiological path length were examined for the five beam angles (see

Table A1. Relative percentage volume of each tissue class in MR_{pCT} and CT_{strat} within the CT body \cap MR body.

Classes	CT _{strat} (%)	MR _{pCT} (%)	<i>p</i> -value
Outside air	0	0	
Fat	45.4 ± 8.5	39.4 ± 8.3	<0.001
Muscle	46.2 ± 7.5	49.9 ± 6.9	<0.001
Spongy bone	6.9 ± 1.2	9.2 ± 1.4	<0.001
Compact bone	1.4 ± 0.4	1.6 ± 0.5	0.2

Table A2. Confusion matrix within CT body \cap MR body of the tissue classification in CT_{strat} versus the percentage of voxels in the body contour intersection that belong to a specific class of MR_{pCT} and of CT_{strat}.

		CT _{strat}			
		Fat	Muscle	Spongy bone	Compact bone
MR _{pCT}	Fat	33.8 ± 8.7	5.5 ± 1.3	0.1 ± 0.1	0.01 ± 0.01
	Muscle	10.8 ± 1.6	38.7 ± 6.9	0.3 ± 0.2	0.05 ± 0.05
	Spongy bone	0.7 ± 0.2	1.8 ± 0.4	6.2 ± 1.0	0.5 ± 0.1
	Compact bone	0.11 ± 0.05	0.3 ± 0.1	0.30 ± 0.09	0.9 ± 0.3

section 2.2) for CT_{strat} and MR_{pCT}. Radiological beam paths were calculated in the treatment planning system (Monaco), using the *Clini* calibration curve. Statistical significance of the radiological path length differences was tested conducting a t-test at $p = 0.01$ significance level.

(1) The mean HU difference over all patients was -8.3 ± 5.2 HU (1 SD), and -12.4 ± 3.3 HU for the body contour intersection between CT_{reg} and MR_{pCT}, and between CT_{strat} and MR_{pCT}, respectively. The corresponding MAE was 57.8 ± 8.0 HU (1 SD), and 36.7 ± 5.9 HU. A double sample t-test for MAE resulted in a p -value < 0.01 , which indicates that the difference between the two populations is statistically significant.

Since the MAE is lower when calculated on CT_{strat} than when calculated on CT_{reg}, we conclude that MR_{pCT} is more similar to CT_{strat} than to CT_{reg}. The value obtained in terms of MAE (36.7 ± 5.9 HU) between CT_{strat} and MR_{pCT} is comparable to the findings reported by Siverson *et al* (2015) (36.5 ± 4.1 HU—in the body contour after non rigid registration).

(2i) Table A1: the result of the volumetric analysis performed in CT_{strat} and MR_{pCT} shows that only the volume of the compact bone class is statistically compatible between the two datasets (see further for possible explanation).

(2ii) Table A2 reports the average and SD of the confusion matrix over all the patients. The classification into tissue classes between MR_{pCT} and CT_{strat} was consistent (sum of the values along the diagonal) for $79.6 \pm 11.2\%$ of the body intersection volume. Misclassification between muscle and fat occurred for $16.3 \pm 2.1\%$ of the body intersection volume. The misclassification may originate from the *set-up & positioning differences*, and the *MR-related geometric inaccuracy* factors, but also from internal motion. Furthermore, misclassification may originate also from the image processing proposed to generate CT_{strat}, in case it does not correctly emulate the voxel content of MR_{pCT}. No statistically significant dose differences were observed due to inter-scan variability (section 3), and the range used to stratify CT_{reg} into tissue classes (table 1) has been arbitrarily chosen. The range could be further optimised, as

well as the image processing proposed to generate CT_{strat} . However, the correct classification rate obtained ($\sim 80\%$) was considered satisfactory.

To understand whether the dissimilarity still present between CT_{strat} and MR_{pCT} may contribute to dose differences, and whether further optimisation of the proposed image processing would be required, we investigated the radiological path lengths. The difference in terms of average over all the patients of the radiological path lengths between CT_{strat} and MR_{pCT} was 0.01 ± 1.14 mm ($p = 0.98$). Thus, we conclude that the proposed image processing enables the generation of CT-based pCT sufficiently similar to MR_{pCT} .

We believe that the results here discussed demonstrate that CT_{strat} and CT_{reg} can be used to estimate the contribution of the *pseudo-CT generation* confounding factor.

References

- Baldwin L N, Wachowicz K, Thomas S D, Rivest R, Fallone B G, Tg A, Wachowicz K, Thomas S D, Rivest R and Fallone B G 2007 Characterization, prediction, and correction of geometric distortion in 3 T MR images *Med. Phys.* **34** 388–99
- Brock K K and Dawson L A 2014 Point: principles of magnetic resonance imaging integration in a computed tomography-based radiotherapy workflow *Semin. Radiat. Oncol.* **24** 169–74
- Chen L, Price R A, Nguyen T B, Wang L, Li J S, Qin L, Ding M, Palacio E, Ma C M and Pollack A 2004 Dosimetric evaluation of MRI-based treatment planning for prostate cancer *Phys. Med. Biol.* **49** 5157–70
- Chernak E S, Rodriguez-Antunez A, Jelden G L, Dhaliwal R S and Lavik P S 1975 The use of computed tomography for radiation therapy treatment planning *Radiology* **117** 613–4
- Constantinou C, Harrington J C and DeWerd L A 1992 An electron density calibration phantom for CT-based treatment planning computers *Med. Phys.* **19** 325–7
- Debois M *et al* 1999 The contribution of magnetic resonance imaging to the three-dimensional treatment planning of localized prostate cancer *Int. J. Radiat. Oncol. Biol. Phys.* **45** 857–65
- Dempsey J, Benoit D, Fitzsimmons J, Haghight A, Li J, Low D, Mutic S, Palta J, Romeijn H and Sjoden G 2005 A device for realtime 3D image-guided IMRT *Int. J. Radiat. Oncol. Biol. Phys.* **63** S202
- Devic S 2012 MRI simulation for radiotherapy treatment planning *Med. Phys.* **39** 6701
- Dirix P, Haustermans K and Vandecaveye V 2014 The value of magnetic resonance imaging for radiotherapy planning *Semin. Radiat. Oncol.* **24** 151–9
- Dixon W T 1984 Simple proton spectroscopic imaging *Radiology* **153** 189–94
- Dowling J A, Lambert J, Parker J, Salvado O, Fripp J, Capp A, Wratten C, Denham J W and Greer P B 2012 An atlas-based electron density mapping method for magnetic resonance imaging (MRI)-alone treatment planning and adaptive MRI-based prostate radiation therapy *Int. J. Radiat. Oncol. Biol. Phys.* **83** e5–11
- Eggers H, Brendel B, Duijndam A and Herigault G 2011 Dual-echo Dixon imaging with flexible choice of echo times *Magn. Reson. Med.* **65** 96–107
- Fallone B G, Murray B, Rathee S, Stanescu T, Steciw S, Vidakovic S, Blosser E and Tymofichuk D 2009 First MR images obtained during megavoltage photon irradiation from a prototype integrated linac-MR system *Med. Phys.* **36** 2084–8
- Fraass B A, McShan D L, Diaz R F, Ten Haken R K, Aisen A, Gebarski S, Glazer G and Lichter A S 1987 Integration of magnetic resonance imaging into radiation therapy treatment planning: I. Technical considerations *Int. J. Radiat. Oncol. Biol. Phys.* **13** 1897–908
- Fransson A, Andreo P and Pötter R 2001 Aspects of MR image distortions in radiotherapy treatment planning *Strahlenther. Onkol.* **177** 59–73
- Helle M, Schadewaldt N, Frantzen-Stenecker M, Schulz H, Stehning C, van der Heide U and Renisch S 2014 Evaluation of Dixon based soft tissue and bone classification in the pelvis for MR-only-based radiation therapy planning *Proc. Int. Soc. Magn. Reson. Med.* **22** 4238
- IAEA 2008 *The Role of PET/CT in Radiation Treatment Planning for Cancer Patient Treatment* (IAEA TECDOC vol 1063) (Vienna: International Atomic Energy Agency)

- ICRU 1989 *Report 44. Tissue Substitutes in Radiation Dosimetry and Measurement* International Commission on Radiation Units and Measurements
- ICRU 1992 *Report 46. Photon, Electron, Proton, and Neutron Interaction Data for Body Tissues* International Commission on Radiation Units and Measurements
- Inness E K, Moutrie V and Charles P H 2014 The dependence of computed tomography number to relative electron density conversion on phantom geometry and its impact on planned dose *Australas. Phys. Eng. Sci. Med.* **37** 385–91
- Johansson A, Karlsson M, Yu J, Asklund T and Nyholm T 2012 Voxel-wise uncertainty in CT substitute derived from MRI *Med. Phys.* **39** 3283–90
- Jonsson J H, Karlsson M G, Karlsson M and Nyholm T 2010 Treatment planning using MRI data: an analysis of the dose calculation accuracy for different treatment regions *Radiat. Oncol.* **5** 62
- Kapanen M, Collan J, Beule A, Seppälä T, Saarilahti K and Tenhunen M 2013 Commissioning of MRI-only based treatment planning procedure for external beam radiotherapy of prostate *Magn. Reson. Med.* **70** 127–35
- Karlsson M, Karlsson M G, Nyholm T, Amies C and Zackrisson B 2009 Dedicated magnetic resonance imaging in the radiotherapy clinic *Int. J. Radiat. Oncol. Biol. Phys.* **74** 644–51
- Khoo V S, Dearnaley D P, Finnigan D J, Padhani A, Tanner S F and Leach M O 1997 Magnetic resonance imaging (MRI): considerations and applications in radiotherapy treatment planning *Radiother. Oncol.* **42** 1–15
- Kim J, Glide-Hurst C, Doemer A, Wen N, Movsas B and Chetty I J 2015 Implementation of a novel algorithm for generating synthetic CT images from magnetic resonance imaging data sets for prostate cancer radiation therapy *Int. J. Radiat. Oncol. Biol. Phys.* **91** 39–47
- Klein S, Pluim J P W, Staring M and Viergever M A 2009 Adaptive stochastic gradient descent optimisation for image registration *Int. J. Comput. Vis.* **81** 227–39
- Klein S, Staring M, Murphy K, Viergever M A and Pluim J P 2010 Elastix: a toolbox for intensity-based medical image registration *IEEE Trans. Med. Imaging* **29** 196–205
- Knöös T, Nilsson M and Ahlgren L 1986 A method for conversion of Hounsfield number to electron density and prediction of macroscopic pair production cross-sections *Radiother. Oncol.* **5** 337–45
- Kohavi R and Provost F 1998 Glossary of terms *Mach. Learn.* **30** 271–4
- Korhonen J, Kapanen M, Keyriläinen J, Seppälä T and Tenhunen M 2014 A dual model HU conversion from MRI intensity values within and outside of bone segment for MRI-based radiotherapy treatment planning of prostate cancer *Med. Phys.* **41** 011704
- Korsholm M E, Waring L W and Edmund J M 2014 A criterion for the reliable use of MRI-only radiotherapy *Radiat. Oncol.* **9** 16
- Lambert J et al 2011 MRI-guided prostate radiation therapy planning: investigation of dosimetric accuracy of MRI-based dose planning *Radiother. Oncol.* **98** 330–4
- Lee Y K, Bollet M, Charles-Edwards G, Flower M A, Leach M O, McNair H, Moore E, Rowbottom C and Webb S 2003 Radiotherapy treatment planning of prostate cancer using magnetic resonance imaging alone *Radiother. Oncol.* **66** 203–16
- Lips I M, Dehnad H, van Gils C H, Boeken Kruger A E, van der Heide U A and van Vulpen M 2008 High-dose intensity-modulated radiotherapy for prostate cancer using daily fiducial marker-based position verification: acute and late toxicity in 331 patients *Radiat. Oncol.* **3** 15
- Mcjury M, O'Neill A, Lawson M, Mcgrath C, Grey A, Page W and O'Sullivan J 2011 Assessing the image quality of pelvic MR images acquired with a flat couch for radiotherapy treatment planning *Br. J. Radiol.* **84** 750–5
- Mijnheer B J, Battermann J J and Wambersie A 1987 What degree of accuracy is required and can be achieved in photon and neutron therapy? *Radiat. Oncol.* **8** 237–52
- Nyholm T and Jonsson J 2014 Counterpoint: opportunities and challenges of a magnetic resonance imaging-only radiotherapy work flow *Semin. Radiat. Oncol.* **24** 175–80
- Nyholm T, Nyberg M, Karlsson M G and Karlsson M 2009 Systematisation of spatial uncertainties for comparison between a MR and a CT-based radiotherapy workflow for prostate treatments *Radiat. Oncol.* **4** 1–9
- Paulson E S, Erickson B, Schultz C and Allen Li X 2015 Comprehensive MRI simulation methodology using a dedicated MRI scanner in radiation oncology for external beam radiation treatment planning *Med. Phys.* **42** 28–39

- Pereira G C, Traughber M and Muzic R F 2014 The role of imaging in radiation therapy planning: past, present, and future *Biomed. Res. Int.* **2014** 231090
- Prior P, Chen X, Botros M, Paulson E S, Lawton C, Erickson B and Li X A 2016 MRI-based IMRT planning for MR-linac: comparison between CT- and MRI-based plans for pancreatic and prostate cancers *Phys. Med. Biol.* **61** 3819–42
- Raaymakers B W, Raaijmakers A J E, Kotte A N T J, Jette D and Legendijk J J W 2004 Integrating a MRI scanner with a 6 MV radiotherapy accelerator: dose deposition in a transverse magnetic field *Phys. Med. Biol.* **49** 4109–18
- Rank C M, Tremmel C, Hünemohr N, Nagel A M, Jäkel O and Greilich S 2013 MRI-based treatment plan simulation and adaptation for ion radiotherapy using a classification-based approach *Radiat. Oncol.* **8** 51
- Rasch C, Barillot I, Remeijer P, Touw A, van Herk M and Lebesque J V 1999 Definition of the prostate in CT and MRI: a multi-observer study *Int. J. Radiat. Oncol. Biol. Phys.* **43** 57–66
- Roach M I, Faillace-Akazawa P, Malfatti C, Holland J and Hricak H 1996 Prostate volumes defined by magnetic resonance imaging and computerized tomographic scans for three-dimensional conformal radiotherapy *Int. J. Radiat. Oncol. Biol. Phys.* **35** 1011–8
- Roberson P L, McLaughlin P W, Narayana V, Troyer S, Hixson G V and Kessler M L 2005 Use and uncertainties of mutual information for computed tomography/magnetic resonance (CT/MR) registration post permanent implant of the prostate *Med. Phys.* **32** 473–82
- Schadewaldt N, Schulz H, Helle M, Frantzen-Stenecker M, Heide U and Renisch S 2014 SU-EJ-141: comparison of dose calculation on automatically generated MRbased ED maps and corresponding patient CT for clinical prostate EBRT plans *Med. Phys.* **41** 188
- Schmidt M A and Payne G S 2015 Radiotherapy planning using MRI *Phys. Med. Biol.* **60** R323–61
- Seco J and Evans P M 2006 Assessing the effect of electron density in photon dose calculations *Med. Phys.* **33** 540–52
- Siversson C, Nordström F, Nilsson T, Nyholm T, Jonsson J, Gunnlaugsson A and Olsson L E 2015 Technical note: MRI only prostate radiotherapy planning using the statistical decomposition algorithm *Med. Phys.* **42** 6090–7
- Skrzyński W, Zielińska-Dabrowska S, Wachowicz M, Slusarczyk-Kacprzyk W, Kukolowicz P F and Bulski W 2010 Computed tomography as a source of electron density information for radiation treatment planning *Strahlenther. Onkol.* **186** 327–33
- Stanescu T, Wachowicz K and Jaffray D A 2012 Characterization of tissue magnetic susceptibility-induced distortions for MRIgRT *Med. Phys.* **39** 7185–93
- Sun J, Dowling J A, Pichler P, Parker J, Martin J, Stanwell P, Arm J, Menk F and Greer P B 2015 Investigation on the performance of dedicated radiotherapy positioning devices for MR scanning for prostate planning *J. Appl. Clin. Med. Phys./Am. Coll. Med. Phys.* **16** 4848
- Sun J, Pichler P, Dowling J, Menk F, Stanwell P, Arm J and Greer P B 2014 MR simulation for prostate radiation therapy: effect of coil mounting position on image quality *Br. J. Radiol.* **87** 20140325
- Thomas S J 1999 Relative electron density calibration of CT scanners for radiotherapy treatment planning *Br. J. Radiol.* **72** 781–6
- Thwaites D 2013 Accuracy required and achievable in radiotherapy dosimetry: have modern technology and techniques changed our views? *J. Phys.: Conf. Ser.* **444** 012006
- Van den Berge D L, Ridder M D and Storme G A 2000 Imaging in radiotherapy *Eur. J. Radiol.* **36** 41–8
- van Herk M, Bruce A, Kroes A P, Shouman T, Touw A and Lebesque J V 1995 Quantification of organ motion during conformal radiotherapy of the prostate by three dimensional image registration *Int. J. Radiat. Oncol. Biol. Phys.* **33** 1311–20
- Villeirs G M, Vaerenbergh K, Vakaet L, Bral S, Claus F, Neve W J, Verstraete K L and Meerleer G O 2005 Interobserver delineation variation using CT versus combined CT + MRI in intensity-modulated radiotherapy for prostate cancer *Strahlenther. Onkol.* **181** 424–30
- Walker A, Liney G, Metcalfe P and Holloway L 2014 MRI distortion: considerations for MRI based radiotherapy treatment planning *Australas. Phys. Eng. Sci. Med.* **37** 103–13
- Wang D, Strugnell W, Cowin G, Doddrell D M and Slaughter R 2004 Geometric distortion in clinical MRI systems: Part I: Evaluation using a 3D phantom *Magn. Res. Imaging* **22** 1211–21